energies

MDPI

*Article*

# Modeling of Grid-Connected PV–Storage System with Frequency Support Capability Under Multi-Mode Control Strategy

**Yi Zhang [1], Weiwei Xu [2,*], Bingyu Weng [3], Yongkai Diao [3] and Pengcheng Yang [1]**

[1] College of Electrical Engineering, Zhejiang University, Hangzhou 310027, China; ypc196@126.com (P.Y.)
[2] Electric Power Research Institute of State Grid Zhejiang Electric Power Co., Ltd., Hangzhou 310014, China
[3] State Grid Ningbo Power Supply Company, Ningbo 315000, China
* Correspondence: vvvvei@126.com

**Abstract**

This study examines coordinated active-power allocation in a DC-coupled photovoltaic (PV) and energy storage system (ESS) with a virtual synchronous generator (VSG) inverter. A rule-based supervisor selects PV maximum power point tracking (MPPT) or the voltage control mode (VCM) and ESS charging, discharging or standby using the available PV power, state of charge (SOC) and categorical scheduling inputs. The implementation combines bounded sampled adaptive inertia, a frequency deadband, measured-current guards and a supercapacitor DC link regulator. Simulations record all five modes and SOC-dependent discharge inhibition under a prescribed source-frequency disturbance. Matched comparisons quantify the scheduling role of PV curtailment, the transient trade-offs of adaptive inertia and the DC link response with the supercapacitor branch retained or removed. Recorded mode states and transient metrics characterize switching behavior. A conditional bound is derived for the reduced frequency state, with parameter and discretization checks defining its evaluation scope. The results characterize five-mode coordination and its response limits in the specified simulation benchmark.

**Keywords:** grid-connected PV–storage system; system architecture design; adaptive VSG; multi-mode switching; Simulink simulation

## 1. Introduction

The increasing penetration of converter-interfaced renewable generation changes the inertial and damping characteristics of power systems and motivates coordinated control of renewable sources and energy storage. Photovoltaic (PV) generation and power-electronic technologies are central to this transition, but their integration also introduces challenges for grid-frequency stability [1].

PV and battery systems interface with the grid through power-electronic converters. Their frequency support behavior depends on the implemented control and available power and energy, rather than on the direct mechanical coupling of a synchronous generator. As converter penetration increases, this distinction motivates explicit consideration of frequency support controls and operating constraints [2].

This study investigates a grid-connected PV–storage control architecture that combines active-power response to frequency disturbances with state-of-charge (SOC) constrained energy storage system (ESS) scheduling. Time-of-use (TOU) period categories and storage operating limits are inputs to a rule-based mode selection process [3]. The scheduling objectives coordinate PV utilization, ESS operation and frequency support.

Check for updates

Academic Editor: JongHoon Kim

Received: 17 September 2026
Revised: 12 October 2026
Accepted: 16 October 2026
Published: 4 November 2026

**Copyright:** © 2026 by the authors. Licensee MDPI, Basel, Switzerland. This article is an open access article distributed under the terms and conditions of the Creative Commons Attribution (CC BY) license.

PV–storage frequency support schemes combine PV power curtailment with ESS power regulation, including droop and VSG control. The authors of [4] combined synthetic inertia and frequency droop control, as illustrated in Figure 1. A filtered frequency signal is used to adjust the active-power reference according to frequency deviation and its rate of change. The resulting support depends on the operating point and available power reserve.

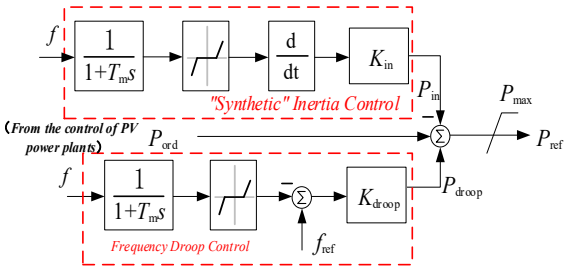



**Figure 1.** Photovoltaic inverter droop control schematic.

The authors of [5] studied a three-port PV–battery–DC link energy router based on an interleaved boost structure and a dual active bridge converter. Its six operating modes classify power flow among the ports and use optimized converter modulation. They are not equivalent to the five SOC- and scheduling-dependent modes considered here. Figure 2 retains a separate six-mode scheduling illustration for background comparison; it does not define the proposed controller states. The authors of [6] addressed PV and load uncertainties through joint sizing and operation of residential PV–battery systems.

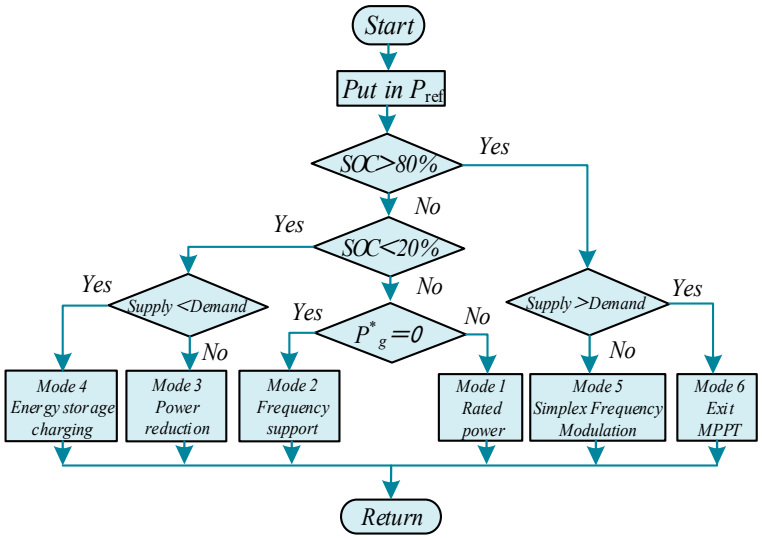



**Figure 2.** Author-redrawn background six-mode scheduling illustration. Its mode labels are distinct from the five-mode definitions used in Table 1. The superscript * denotes a reference value.

Prior multi-mode schemes address TOU-based PV–storage management [3], optimized three-port power routing [5] and grid-connected and islanded energy management [7]. The present framework organizes PV MPPT and VCM selection and SOC-constrained ESS allocation around a shared DC-coupled VSG inverter and a supercapacitor regulator. Its contribution is an explicit implementation and evaluation of this coordination under stated source and converter constraints. Equation (7) adopts an existing inertia law. Matched comparisons examine the allocation rule and inertia component separately from the complete schemes in [3,7].

**Table 1.** Summary of the five operating modes and their scheduling contexts.

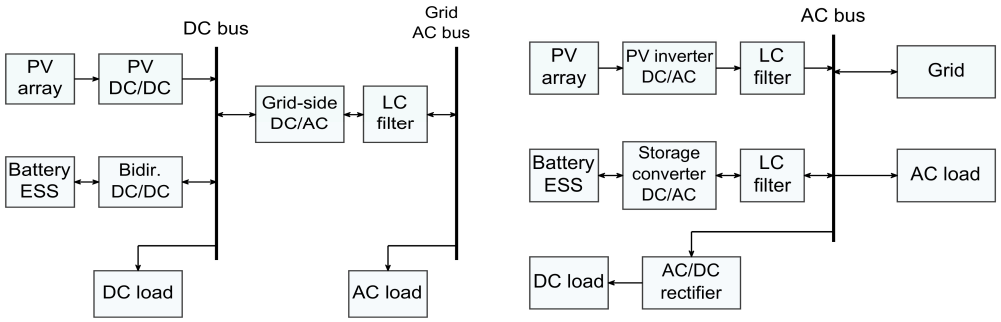
| Mode | PV Control | ESS Scheduling State | SOC Context |
|---|---|---|---|
| 1 | MPPT | Charging within the available envelope | Below 80%; PV surplus charging or an off-peak charging request. |
| 2 | VCM | Charging at the available envelope | Below 80%, with PV surplus above the ESS charging limit. |
| 3 | VCM | Standby | SOC ≥ 80%; PV surplus in peak or shoulder context. |
| 4 | MPPT | Standby in normal operation; frequency response subject to SOC limits | Peak SOC ≤ 30%; off-peak SOC ≥ 80%; shoulder PV deficit. Below 20%, no discharge. |
| 5 | MPPT | Discharging | Above 30% in the peak-period power deficit case. |

The grid-side inverter retains VSG control in every mode. SOC ≥ 80% prohibits charging, and SOC < 20% prohibits commanded discharge. Mode 4 provides base scheduling standby for peak-period SOC ≤ 30%, off-peak SOC ≥80% and a shoulder-period PV deficit. The shoulder category prohibits discharge at every SOC. Consequently, a constrained PCC injection request may remain unmet.

## 2. Topology Design and Control Strategy

### *2.1. Topology Selection*

Two typical configurations are commonly adopted for integrating PV generation with energy storage systems: a DC-coupled configuration, in which the PV and energy storage units are connected to a common DC link and share the grid-side inverter, and an AC-coupled configuration, in which the PV and storage units are interfaced with the grid through separate power converters [7–9]. As shown in Figure 3a, the DC-coupled configuration provides a high level of integration and enables coordinated power management through the common DC bus. In contrast, the AC-coupled configuration shown in Figure 3b provides greater modularity and allows the PV and energy storage units to be controlled and operated more independently. Therefore, the selection of the coupling architecture depends on system-level requirements such as integration, control flexibility, expandability, and coordinated power management.




(**a**) (**b**)

**Figure 3.** PV–storage topologies: (**a**) shared DC link and inverter (DC-coupled); (**b**) separate converters on an AC bus (AC-coupled). Blocks label conversion types; arrows show possible power flow.

### 2.2. Control Strategy

At the converter level, grid-following (GFL) control and grid-forming (GFM) control differ in how their terminal electrical variables and synchronization are regulated. Coordinated GFL and GFM operation can support PV–storage integration [10]. Conventional GFL control typically synchronizes to an external voltage waveform, whereas GFM control establishes an internal voltage reference and can provide active-power response through its power synchronization dynamics [11]. These converter functions operate alongside PV-side MPPT and VCM control and ESS energy scheduling, whose available reserves depend on the operating point and constraints.

In this paper, the PV-side DC/DC converter uses maximum power point tracking (MPPT) or the voltage control mode (VCM), while the grid-side inverter uses VSG-based grid-forming control. In a synchronous generator, active power–frequency regulation is completed by the governor system, composed of the governor and the prime mover. In VSG control, the speed regulation process is simplified, and only the basic principles are introduced. The active power–frequency system of VSG needs to achieve automatic distribution of active power among the micro-sources such that

$$P_{ref} - P_m = K_p(\omega - \omega_0) \tag{1}$$

In the formula, $\omega_0$ is the reference angular velocity, $P_{ref}$ is the reference power, $\omega$ is the angular velocity, $P$ is the active power output of the VSG, and $K_p$ is the droop coefficient of the prime mover.

Using a second-order model, the relationship between the output angular frequency and output power of the VSG is

$$\begin{cases} J\frac{d\omega}{dt} = \frac{P_m}{\omega_m} - \frac{P}{\omega_m} - D(\omega - \omega_0) \\ \frac{d\delta}{dt} = \omega \end{cases} \tag{2}$$

In the formula, $\omega_m$ is the mechanical angular velocity, $J$ is the virtual inertia of the rotor (kg·m$^2$), $D$ represents the damping coefficient, $\omega_0$ represents the speed corresponding to the reference frequency, $P_m$ represents the mechanical power, and $\delta$ is the output power angle. The algorithm structure flowchart is shown in Figure 4.

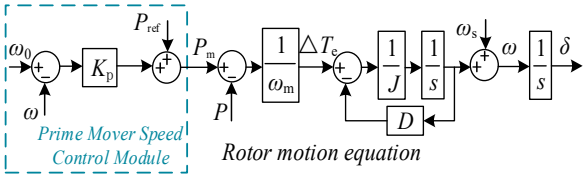



**Figure 4.** Droop control schematic.

Since the VSG operates near the reference speed point, the influence of speed variations on the damping winding can be neglected, which can be approximately expressed as $\omega_m \approx \omega_0$, $\omega_s \approx \omega_0$. Therefore, the system frequency variation and power variation can be simplified as follows:

$$\frac{\omega - \omega_0}{P - P_{ref}} = -\frac{1}{J\omega_0 s + D\omega_0 + K_p} \tag{3}$$

To maximize solar energy utilization, PV systems generally operate at the maximum power point under normal operating conditions. However, strict MPPT operation leaves a limited upward active-power reserve, thereby restricting the capability of the PV system to increase its power output in response to a frequency decrease. To enable active frequency support, the PV array can be operated in a de-loaded condition by shifting its operating point away from the maximum power point and maintaining a predefined active-power

reserve [12]. When a power imbalance causes grid-frequency deviations, the reserved PV power can be rapidly released or adjusted according to the frequency support requirement. Therefore, coordinated operation between maximum-power extraction and de-loaded control provides a means of balancing PV energy utilization and grid support capability. The corresponding PV de-loaded operating characteristic is illustrated in Figure 5.

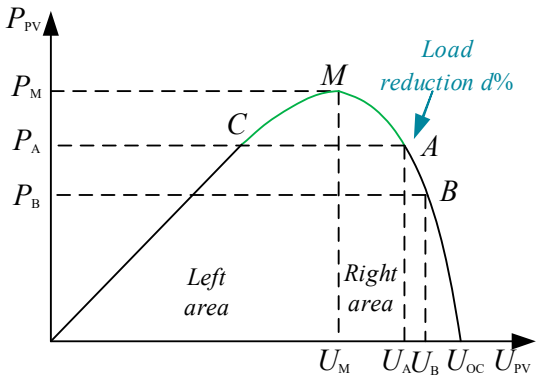



**Figure 5.** PV de-loaded operating characteristic.

## 3. Control Scheme Design

### *3.1. Single-Mode Control Scheme*

Based on the topology comparison discussed above, and considering the coordinated control requirements of the PV generation, energy storage system and grid-side converter, this paper adopts a DC-coupled PV–storage architecture with a common DC bus. In this configuration, the PV array, energy storage unit, and supercapacitor are coupled through the DC link, which facilitates coordinated power management among different energy sources and enables the energy storage and supercapacitor to compensate for the instantaneous power imbalance between the PV source and the grid-side converter. Meanwhile, the common grid-side inverter provides a unified interface for implementing VSG control and active frequency support. Therefore, the selected topology is well suited to the subsequent multi-mode control strategy involving PV MPPT and VCM switching, energy storage charging and discharging, DC-bus voltage regulation and grid-frequency support.

In the single-mode configuration, the PV array operates under MPPT control, with a PI-based voltage loop regulating the PV-side operating point. The common grid-side inverter uses VSG control to provide the underlying active-power and frequency control structure. The multi-mode supervisor builds on this converter control structure.

### *3.2. Multi-Mode Control Scheme*

The supervisory controller uses predefined threshold rules to switch the PV-side converter between MPPT and VCM and schedule the ESS among charging, discharging and standby states. The rules depend on the SOC, available PV power relative to requested PCC active-power injection, ESS power limits and TOU period category. The supercapacitor branch assists with DC-link voltage regulation. Figure 6 shows the PV selection and base ESS scheduling logic.

The supervisory rules use TOU period labels, ESS SOC, PV power availability and requested PCC active-power injection. The intended usable SOC range is 20–80%, with charge and discharge power limits. In peak- or shoulder-period PV-surplus operation, when PV generation exceeds the requested PCC injection, and the surplus power is greater than the maximum charging power of the energy storage system, the allocator requests charging at the available envelope. If the surplus power is less than the maximum charging power,

then it requests charging at the surplus power. Similarly, for permitted peak-period base discharge, if $P_g - P_{PVmax} > P_{ESSmax}$, then the allocator requests discharge at $P_{ESSmax}$ power; if $P_g - P_{PVmax} < P_{ESSmax}$, then the allocator requests the remaining deficit within its envelope.

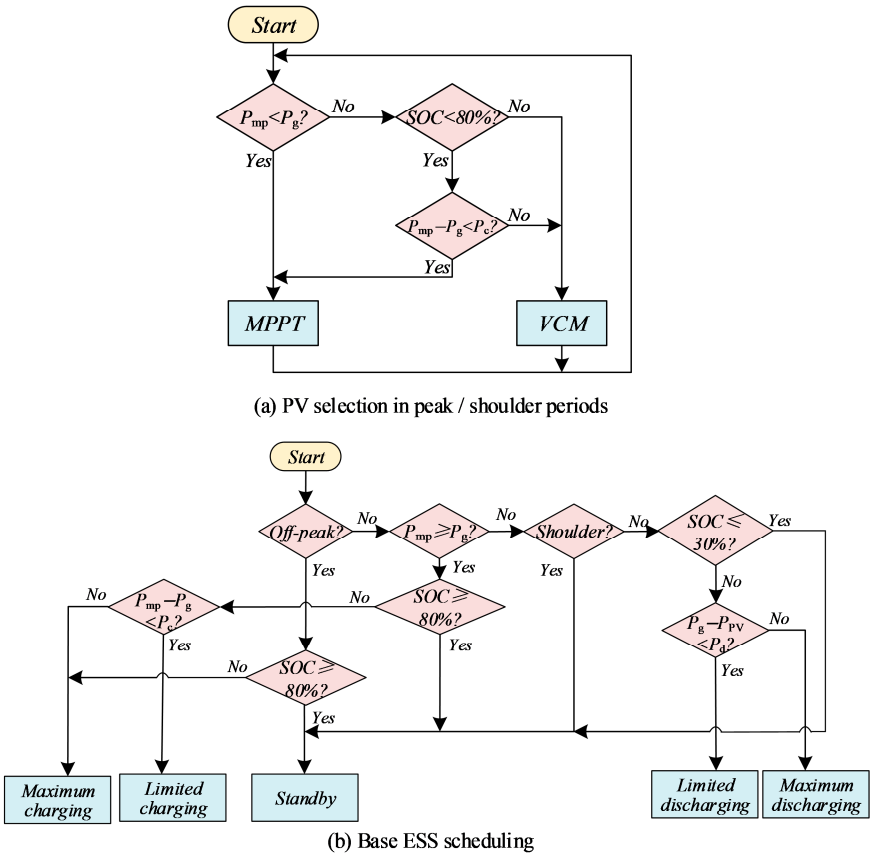



**Figure 6.** Rule-based PV selection and base ESS scheduling: (**a**) PV selection during peak and shoulder periods and (**b**) base ESS scheduling. Off-peak operation selects MPPT. $P_{mp}$ is the estimated available PV maximum; $P_c$ and $P_d$ are the available charging and discharging DC envelopes, respectively. Frequency allocation and final SOC or current guards follow Section 4.3. Arrows indicate control-flow direction; node colors distinguish the start, decision and action blocks.

#### 3.2.1. Peak-Period Control Strategy

The peak-period category coordinates PV–storage injection with the requested PCC active power. The control logic is as follows:

- PV power supply surplus scenario: $P_{PVmax} > P_g$.
- Energy storage below 80% SOC: Mode 1 maintains MPPT when the available PV surplus is below the charging envelope and requests bounded charging. At or above that envelope, Mode 2 requests the maximum permitted charging and switches PV to the VCM to regulate scheduled injection. The final frequency response and measured terminal power remain subject to the protection and conversion limits in Section 4.3.
- Energy storage at or above 80% SOC: Mode 3 inhibits charging, holds the base ESS scheduling request at zero, and uses the VCM to set the scheduled PV power to the PCC request. Frequency response can release a curtailed PV reserve under the implemented limits.
- PV power supply loss scenario: $P_{PVmax} < P_g$.

For a peak-period PV deficit, the scheduler uses a chosen 30% SOC margin to reserve the 20–30% range for frequency support, while continuous deficit compensation is permitted above 30%:

- Mode 4 (peak-period reserve or protected zone, SOC $\leq$ 30%): The base ESS scheduling request is zero. Within 20% $\leq$ SOC $\leq$ 30%, the frequency response may charge or discharge, subject to the direction-specific power and current envelope. Discharge is inhibited when SOC $<$ 20%. PV remains under MPPT. A $\pm$0.02 Hz frequency deadband in the implemented controller suppresses near-nominal frequency support requests.
- Mode 5 (healthy power level zone, SOC $>$ 30%): The ESS actively discharges to compensate for power shortages, while the PV system maintains MPPT operation to maximize output.

#### 3.2.2. Off-Peak-Period Control Strategy

The off-peak category requests ESS charging. The off-peak transition case retains the PV deficit condition $P_{PVmax} < P_g$.

During off-peak periods, the scheduling rule selects MPPT and requests ESS charging within the available envelope below an 80% SOC. The frequency response and command protection can modify the applied request. The charging power source follows the PCC power balance. The SOC-dependent rules are as follows:

- Charging mode (SOC $<$ 80%): Mode 1 selects MPPT and requests charging at the available scheduling envelope.
- Standby mode (SOC $\geq$ 80%): Mode 4 inhibits charging at the upper boundary. Any additional frequency response follows the SOC, direction and current constraints.

#### 3.2.3. Shoulder-Period Control Strategy

During shoulder periods, the scheduling rule permits charging within the available envelope below an 80% SOC and prohibits commanded discharge at every SOC. Charging is inhibited at or above 80%. A PV deficit selects Mode 4; the PV surplus uses the same SOC- and envelope-dependent selection as the peak context.

The shoulder-period charging-only rule makes charging reduction the available upward ESS response. With insufficient PV and prohibited ESS discharge, a separate local-load deficit would require the external grid or another source. The benchmark evaluates a PCC injection request rather than local-load supply.

PV operation at MPPT in Modes 1, 4 and 5 maintains no deliberate upward PV reserve. Support is obtained from permissible ESS power change, including reduced charging. In VCM Modes 2 and 3, a curtailed PV reserve is allocated first, and the permissible ESS reserve supplies any remainder. The upward ESS reserve is the available discharge envelope minus the scheduled ESS power, and the downward reserve is the scheduled ESS power plus the available charging envelope. These are requested DC-side reserves. The measured PCC response is evaluated separately because conversion, filter and DC-link energy affect its transient value.

## 4. Simulation Modeling of PV–Storage Grid-Connected System

### *4.1. PV–Storage System Model*

The current–voltage relationship of a PV array under varying environmental conditions is expressed as follows:

$$I = I_{sc}\left[1 - C_1\left(e^{\frac{V-dV}{C_2 V_{oc}}} - 1\right)\right] + dI \tag{4}$$

The PV model used a user-defined module with 60 cells, a 213.15 W rated maximum power, a 36.3 V open-circuit voltage, a 7.84 A short-circuit current and a 29 V/7.35 A rated maximum power point. The array comprised 30 series modules in each of 32 parallel strings. Its open-circuit voltage and short-circuit current temperature coefficients were

−0.36099%/°C and +0.102%/°C, respectively. Figures 7 and 8 show the native PV-array characteristics for these parameters.

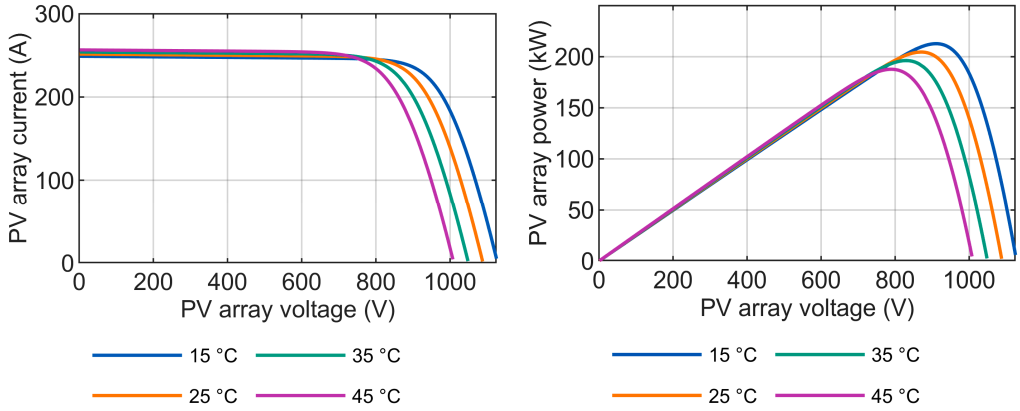



**Figure 7.** Current-model PV-array current–voltage (**left**) and power–voltage (**right**) characteristics at 1000 W/m$^2$ and cell temperatures of 15–45 °C.

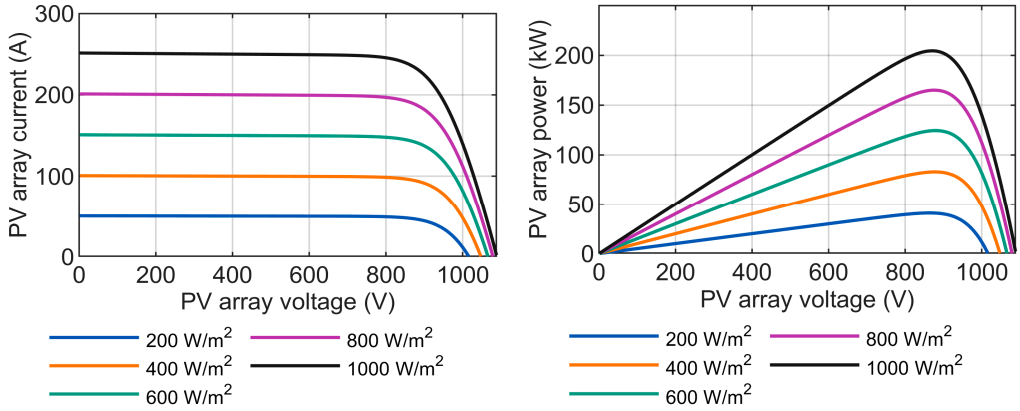



**Figure 8.** Current-model PV-array current–voltage (**left**) and power–voltage (**right**) characteristics at 25 °C and irradiances of 200–1000 W/m$^2$.

For the specified PV model, the peak powers in Figure 7 are 212.595, 204.427, 196.081 and 187.565 kW at 15, 25, 35 and 45 °C, respectively. The maximum-power voltage decreased as the cell temperature rose. In Figure 8, the peak powers increased from 40.763 to 204.427 kW over 200–1000 W/m$^2$. At 800 W/m$^2$ and 25 °C, the static maximum power point was 875.721 V and 164.926 kW, consistent with the preset values used in the matched inertia comparison.

The MPPT controller used the measured voltage and power in the voltage reference P&O shown in Figure 9. Its 0.1 s updates perturbed the reference by 1 V within 750–1050 V. The measured voltage PI uses proportional and integral gains of 0.5 and 1, respectively, duty bounds [0, 1] and clamping anti-windup. P&O perturbations are suspended during VCM. The known-model MPP voltage at 25 °C initialized the controller and its return to MPPT.

The VCM estimated the available PV maximum power from native curves at known irradiance and 25 °C over 200–1000 W/m$^2$. The requested fraction selected the decreasing right-of-MPP branch. The requested de-loading was 100(1 − requested PV power/estimated maximum PV power)%. A 1 ms measured-power correction used proportional and integral gains of 0.001 V/W and 0.01 V/(W·s), respectively, an integral voltage offset bounded to ±80 V and reference bounds from model $V_{mpp}$ + 1 V to $V_{oc}$ − 0.5 V. This correction was enabled after 0.4 s. The bounds selected the reference branch; the measured voltage could

depart from it during transients. The evaluation used the stated irradiance range and a fixed temperature.

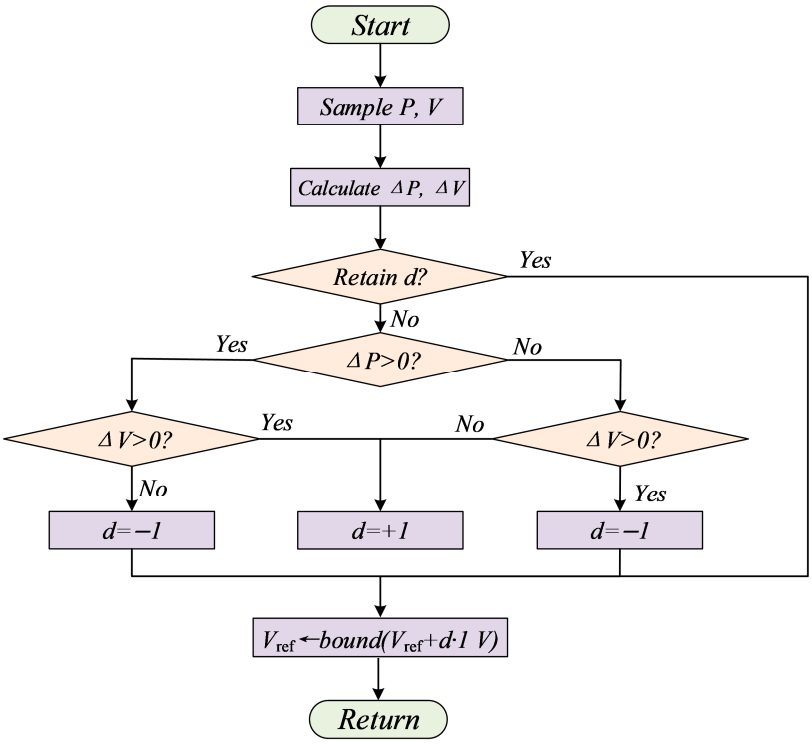



**Figure 9.** Voltage reference P&O for eligible 0.1 s updates from 0.5 s. Retain d applies when the power change magnitude is at most 0.5 W or the voltage change magnitude is at most 0.05 V; the common update still proceeds. VCM gating, initialization and bounds follow Section 4.1. Arrows indicate the algorithm flow; node shading distinguishes the start/end, decision and calculation/update blocks.

Nowadays, battery energy storage systems have begun to be widely applied in various fields, including frequency regulation, grid stabilization, reduction of transmission losses, enhancement of grid reliability, mitigation of generation fluctuations, provision of spinning reserve capacity, peak shaving and valley filling and load balancing [13].

The uniform model uses a lithium-ion battery with a nominal voltage of 1200 V and capacity of 5000 Ah, coupled through a bidirectional Buck–Boost converter. The generic nonlinear supercapacitor block uses C = 100 F, DC resistance of 0.0089 Ω, a voltage parameter of 1200 V, $N_s = 30$, $N_p = 2$ and an initial voltage of 1200 V. The common DC-link capacitor is 0.2 F, with two 0.04 F split capacitors, and its regulator reference is 1500 V. These parameters define the simulation benchmark. The peak, off-peak and shoulder categories are coded as 1, 2 and 3, respectively.

The actual battery SOC feeds the discharge command gate, which prohibits discharge below 20%. The shared controller also applies the upper-SOC and shoulder-period rules. The battery-capacitor and voltage-source initial conditions used the same initial battery voltage. The response simulations use the uniform coupled controller with an explicitly recorded SOC and mode state.

### *4.2. Grid-Connected Control Model*

The grid-side converter uses a conventional VSG model and the adaptive inertia law in Equation (7), following [14]. The supplied model snapshot originally applies a fixed inertia $J = 2$. Separate copies implement fixed and regularized, bounded adaptive inertia for the matched comparison. For Equations (5) and (6), $K_s = \partial P_e / \partial \delta$ at the operating point denotes the local synchronizing power slope in W/rad. Linearizing the implemented torque path

model at a fixed nominal grid frequency gives Jω0 $\Delta\delta^{\cdot\cdot}$ + (Dω0 + $K_p$)$\Delta\delta^{\cdot}$ + Ks$\Delta\delta$ = $\Delta$Pref. This retains the physical power scale; no unity-slope normalization is assumed. The reduced model neglects inner voltage and current dynamics, converter saturation and PV and ESS dynamics:

$$\frac{\Delta\delta(s)}{\Delta P_{ref}(s)} = \frac{1}{J\omega_0 s^2 + \left(D\omega_0 + K_p\right)s + K_s} \tag{5}$$

The pole locations are expressed as follows:

$$s = \frac{-\left(D\omega_0 + K_p\right) \pm \sqrt{\left(D\omega_0 + K_p\right)^2 - 4J\omega_0 K_s}}{2J\omega_0} \tag{6}$$

For the reduced fixed-parameter model, $J > 0$, $\omega_0 > 0$, $D\omega_0 + K_p > 0$ and $K_s > 0$ place both poles in the left half-plane. This result concerns the stated local linearization:

$$J = J_0 + \mu_J \mathrm{sgn}(\omega - \omega_0)\frac{d\omega}{dt} \tag{7}$$

In the formula, $J_0$ is the base value of the moment of inertia, and $\mu_J$ is the adjustment coefficient. When $\mu_J$ is zero, the adaptive moment of inertia control strategy degenerates into a fixed moment of inertia control strategy, where $J$ is the moment of inertia applied in the actual VSG, $\omega$ is the angular frequency output by the VSG and $\omega_0$ is the rated angular frequency. Here, sgn(·) denotes the sign function, with sgn(0) = 0.

For the additional adaptive implementation, the angular-frequency deviation $e$ is sampled every 1 ms. The discontinuous sign term is replaced by tanh($e$/0.01), with $e$ in rad/s. Its derivative is estimated by $q[k]$ = a $q[k-1]$ + b($e[k] - e[k-1]$), where a = exp(−0.001/0.02), b = (1 − a)/0.001 and $q$ is initialized to zero. The raw request $J_0$ + 0.4 tanh($e$/0.01)$q$ uses $J_0$ = 2 kg·m$^2$, is saturated to [0.5, 6] kg·m$^2$ and is limited to a maximum change of 0.02 kg·m$^2$ per 1 ms update, starting from 2 kg·m$^2$. The applied inertia is held between updates. These regularization settings are newly specified for this validation and are not reconstructed historical settings.

The applied inertia update moves by the clipped difference toward the saturated request. Since its initial value and every request lie in [0.5, 6] kg·m$^2$, each update lies between the preceding value and the request; induction therefore preserves positivity and these bounds. Its per-update change is also bounded by construction. Five controller-level checks—zero deviation, small 200 Hz noise, positive and negative ramps and a large 5 Hz cycle—confirm finite inertia values as well as the stated bounds and increment limit. These checks concern the inertia sequence only. A continuous-time energy argument based on a differentiable $J$ cannot be applied directly to this sample-and-hold implementation.

A conditional reduced-frequency bound complements the inertia sequence bounds. Let $e$ be the angular-frequency deviation from the fixed nominal frequency, where c = $D + K_p/\omega_0 > 0$ and $u = (P_{ref} - P_e)/\omega_0$. Let $\sigma$ be one when angular acceleration is applied and zero when reference limiting holds the angular-frequency integrator input at zero. The implemented reduced state then satisfies

$$J(t)\dot{e}(t) = \sigma(t)[u(t) - ce(t)] \tag{8}$$

Assume that $|u(t)| \le$ U and the piecewise held inertia is in [0.5, 6] kg·m$^2$, with a continuous $e$ across inertia updates and reference-limit transitions. We define the accumulated active damping by

$$A(t) = \int_0^t \frac{\sigma(\tau)c}{J(\tau)}d\tau \tag{9}$$

An integrating factor solution and the triangle inequality give the following bound:

$$\begin{aligned} |e(t)| &\le |e(0)|exp[-A(t)] + \tfrac{U}{c}\{1 - exp[-A(t)]\} \\ &\le max\{|e(0)|, \tfrac{U}{c}\} \end{aligned} \tag{10}$$

The reduced frequency state remains bounded under the stated bounded-input assumption without differentiating the sample-and-hold inertia. For a constant $u$ and A(t) increasing without a bound, $e$ converges to $u/c$; the permanent integrator hold does not imply this convergence. These results concern the reduced frequency dynamics and assume bounded electrical forcing. They do not prove bounded forcing from the electrical feedback or stability of the full hybrid electrical system.

Figure 10 uses the same electrical model, initial SOC of 50%, constant environmental inputs, reference disturbance and implemented limits for both inertia settings. The grid source was a 380 V line-to-line RMS at 50 Hz, and the DC-link reference was 1500 V. The simulation ran to 2.2 s with 10 µs signal recording and Tustin switching-event interpolation with continuous PWM and ode23tb. Both cases settled within 150 kW ± 0.6 kW during 1.1–1.2 s before the reference step. The post-step metrics for 1.2–2.2 s are reported with the inertia-comparison results. This was an inertia component test with unchanged upstream scheduling and preset PV references, rather than a comparison of complete supervisory strategies.

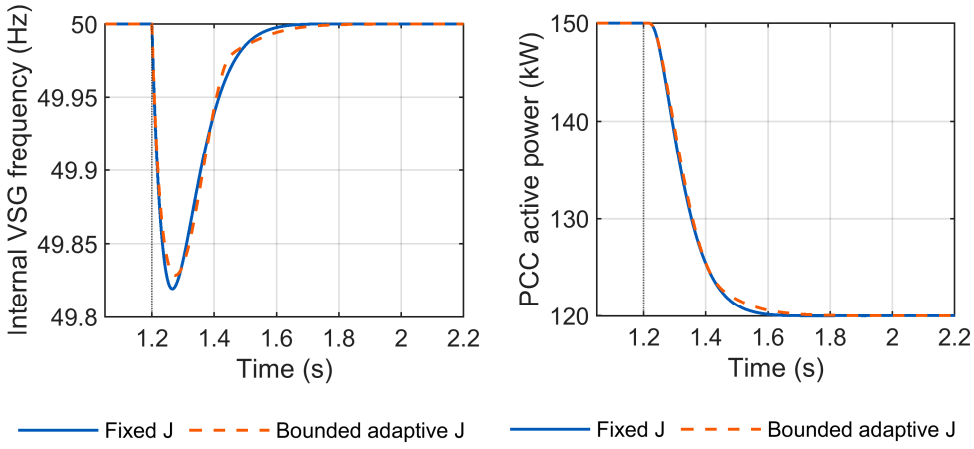



**Figure 10.** Matched inertia component comparison: internal VSG frequency (**left**) and filtered PCC active power (**right**). The reference changed from 150 to 120 kW at 1.2 s. The network voltage source remained at 50 Hz in both cases.

Table 2 lists the retained model parameters and the damping value used in the additional comparison [14,15]. The torque path damping coefficient $D = 70$ replaced the historical, differently scaled value. The stored $S_B$ and $U_B$ parameters were retained for traceability; per-unit scaling was disabled in the PCC voltage and current measurements, and thus $U_B$ is not the physical grid-source voltage. The adaptive implementation parameters are given above.

**Table 2.** Model parameters used or retained in the additional inertia comparison.

| Variable | Description | Value |
|---|---|---|
| $C_f$ | Circuit capacitor | 0.01 mF |
| $L_f$ | Circuit inductance | 0.004 H |
| $R_f$ | Circuit resistance | 0.05 Ω |
| $S_B$ | Stored base power; PCC per-unit scaling disabled | 1 MW |

**Table 2.** *Cont.*

| Variable | Description | Value |
|---|---|---|
| $U_B$ | Stored base voltage; PCC per-unit scaling disabled | 6600 V |
| $D$ | VSG torque-path damping coefficient | 70 N·m·s/rad |
| $f_n$ | Rated frequency | 50 Hz |
| $K_p$ | Droop coefficient | 0.5 |
| $\omega_0$ | Rated angular frequency | $100\pi$ rad/s |
| $\mu_J$ | Adjustment factor | 0.4 |
| $J_0$ | Initial moment of inertia | 2 kg m$^2$ |

### *4.3. Implemented Allocation and Protection*

The scheduling input $P_g$ is a requested PCC active-power injection and not a measured local load. $P_e$ is the filtered PCC AC power. $P_{pv}$ and $P_{ESS}$ are the measured PV and battery terminal DC powers, respectively. Positive storage power denotes discharge. The symbolic $P_{ESSmax}$ in the scheduling rules denotes the available direction-specific DC envelope; it is distinct from the retained 50 kW battery terminal limit. Every 1 ms, the allocator sampled the actual SOC, battery voltage, measured PV power, known-model available PV power, PCC frequency and categorical scheduling input.

The three-phase PCC PLL was sampled at 0.1 ms after normalization via the nominal $380\sqrt{(2/3)}$ V phase peak. Its gain parameters were (180, 3200, 1), an output filter of 25 Hz and a rate limit of 12 Hz/s. A further 20 ms filter acted on deviation from 50 Hz. The frequency-power request uses the steady torque damping or droop slope with a continuous $\pm 0.02$ Hz deadband. The VSG reference compensates for the steady damping or droop contribution already present in the torque path; transient tracking is evaluated from the measured PCC power.

The signed ESS current PI was sampled at 0.1 ms, with proportional and integral gains of 0.004 and 0.5, respectively, conditional integration, integral limits of $\pm 0.4$ and duty limits of $[0, 0.98]$. Steady power-to-current conversion included the actual 3 Ω battery-side RL resistance. The requested current was 84% of the smaller of 50 A and 50 kW/$|V_{battery}|$, with a 45 kW DC request cap. The separate 20 µs measured-current guard tripped and released at 90% and 86% of the terminal envelope, respectively, and blocked simultaneous charge and discharge commands. Inductive and capacitive transient energy was not treated as steady resistive loss.

The inverter dq-current reference was vector-limited to 97% of the independently logged provisional test envelope. The inner PI axes were limited to $\pm 600$ A with clamping and tracking gain of 50. During reference limiting, the inputs to the outer reactive-power and voltage integrators and VSG angular acceleration were held at zero, retaining their states and phases. Uniform cases used a constant 500 A envelope. A separate fixed-inertia $J = 2$ and fixed 50 Hz test reduced the envelope from 500 to 300 A at 1.2 s and released it at 1.4 s. Its measured current and recovery results are discussed in Section 5.3; Supplementary Section S2 provides the complete record summary.

MATLAB's Simulink R2024a executed the simulations from saved model copies. Generative AI assistance through OpenAI Codex (GPT-6, October 2026) was used to prepare the text revision, implement and inspect simulation and analysis scripts and organize validation. Figures were plotted from numerical outputs of the physical model simulations. Model copies, inputs, raw recordings, scripts and all completed checks were retained for reproducibility.

## 5. Simulation Verification Results and Analysis

The experiments used a uniform coupled implementation with bounded adaptive inertia, a frequency deadband, measured ESS guards and inverter reference limiting. The single-mode cases apply a prescribed source-frequency change from 50 to 49.8 Hz at 1.2 s and recovery to 50 Hz at 1.6 s over a 2.2 s run. Each case used constant irradiance, a cell temperature of 25 °C and an explicitly initialized physical SOC. The internal VSG frequency and measured PCC frequency were logged separately; the source-frequency trajectory was an input.

All traces retained their physical units and original simulation timestamps, which were recorded every 10 µs without waveform smoothing or time stretching. The physical and controller settings and initial conditions were retained from the uniform implementation; powergui used Tustin switching-event interpolation with continuous PWM and ode23tb. The separate measured current guard retained its 20 µs control period. The earlier saved out.slx file and common TBE records remained in the audit archive. The three comparison windows were 1.1–1.2 s (A), 1.4–1.5 s (B) and 2.1–2.2 s (C). The reported medians describe these windows; B was not assumed to be fully settled. Each case is one numerical record without independent replications or confidence intervals.

### *5.1. Single-Mode Frequency Response*

#### 5.1.1. Mode 1

Figure 11 shows the Mode 1 response. At an initial SOC of 50% and irradiance of 800 W/m$^2$, the recorded mode remained Mode 1. The PCC-power medians in A, B and C were 150.079, 178.769 and 150.375 kW, respectively. The PV remained in MPPT and approximately constant, while the battery-terminal medians changed from −13.772 to 9.596 and back to −13.709 kW. Increased injection used ESS charging reduction followed by discharge; no deliberate upward PV reserve was assumed. The window B median PCC tracking error relative to the instantaneous allocated target was 5.145 kW.

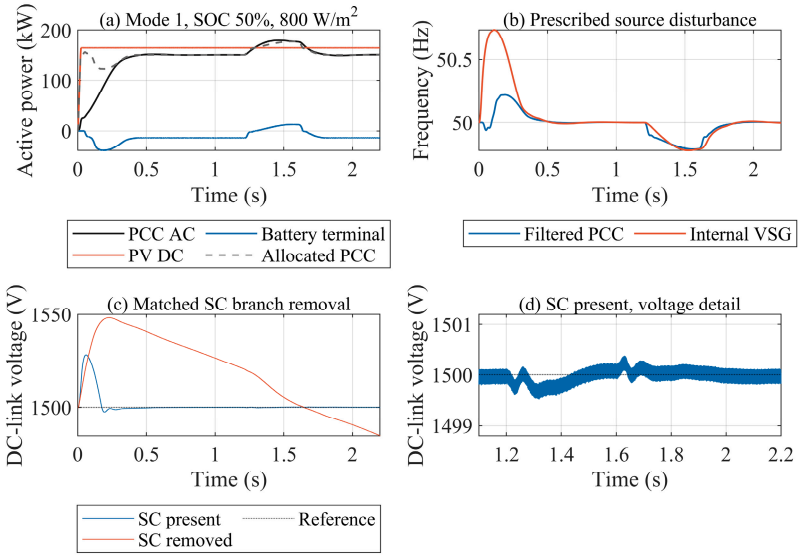



**Figure 11.** Uniform Mode 1 response: (**a**) active power; (**b**) filtered measured PCC and internal VSG frequency; (**c**) matched supercapacitor branch removal DC-link comparison; and (**d**) voltage detail with the branch retained. Negative battery power denotes charging. Panels (**c**,**d**) use the separately matched branch removal pair.

#### 5.1.2. Mode 2

Figure 12 shows the Mode 2 response. At an initial SOC of 50% and irradiance of 1000 W/m$^2$, the recorded mode remained Mode 2. The PCC-power medians in A, B and C were 150.081, 178.770 and 150.378 kW, respectively. The PV used VCM, releasing a curtailed reserve before reducing ESS charging. The PV medians in A and B were 195.094 and 202.609 kW while the battery-terminal medians were −41.847 and −29.319 kW, respectively. Right-branch reference selection is not an instantaneous measured-voltage guarantee near the static MPP.

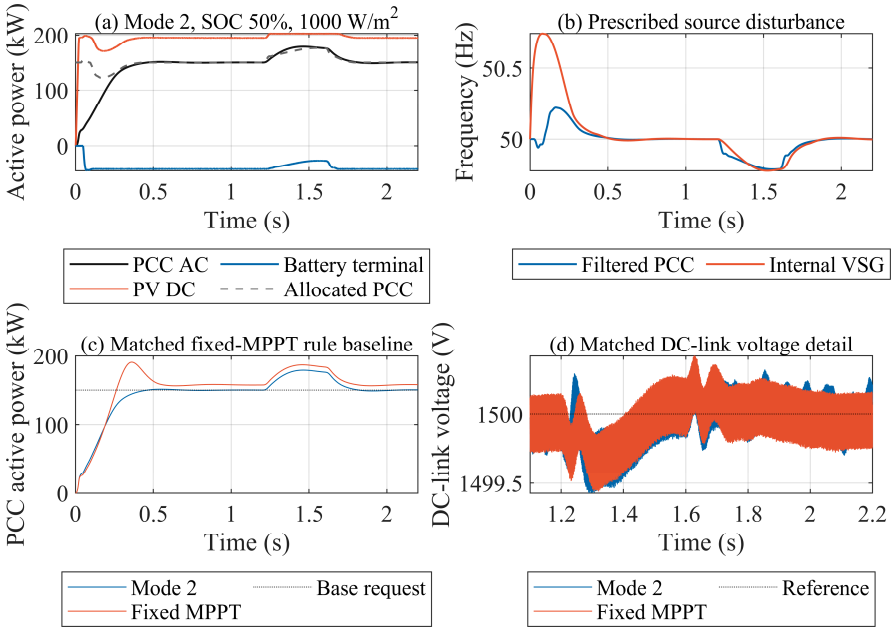



**Figure 12.** Uniform Mode 2 response: (**a**) active power; (**b**) filtered measured PCC and internal VSG frequency; (**c**) PCC power compared with the matched fixed-MPPT rule; and (**d**) matched DC-link voltage detail. The 150 kW line is the base scheduling request.

#### 5.1.3. Mode 3

Figure 13 shows the Mode 3 response. At an initial SOC of 85% and irradiance of 1000 W/m$^2$, the recorded mode remained Mode 3. The PCC-power medians in A, B and C were 150.078, 178.766 and 150.376 kW, respectively. At this upper SOC condition, charging was prohibited, and the ESS current request was zero. VCM provided the allocated reserve; the PV medians in A, B and C were 150.020, 173.596 and 149.977 kW, respectively. The final-window PV median target error was −0.015%. This is a median target error rather than energy conversion efficiency or a bound on all transient samples.

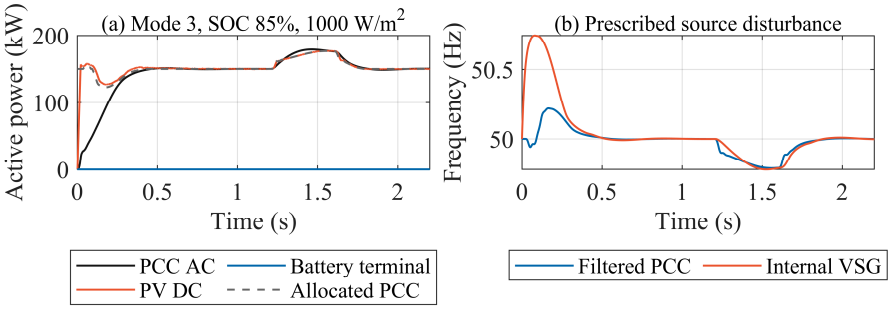



**Figure 13.** Uniform Mode 3 response at initial SOC of 85%: (**a**) active power and allocated PCC target and (**b**) filtered measured PCC and internal VSG frequency. The ESS current request is zero.

#### 5.1.4. Mode 4

Figure 14 shows the Mode 4 response. At an initial SOC of 25% and irradiance of 600 W/m$^2$, the recorded mode remained Mode 4. The PCC-power medians in A, B and C were 124.072, 151.408 and 124.131 kW, respectively. Above the 20% discharge boundary, the ESS supplied the frequency response while its base scheduling request remained zero. The 150 kW base request remained unmet at a normal frequency, with the MPPT PV supplying approximately 124.046 kW. In A and C, the allocated frequency request and both applied PWM directions were zero; the battery-terminal power was about 13.45 W from native passive conduction. At an initial SOC of 19%, the applied discharge command and additional allocated support in B were zero, while the battery terminal median was 13.12 W. These were separate initialized SOC cases. A shoulder-period case at an SOC of 50% and 600 W/m$^2$ also recorded zero for the discharge PWM and no positive ESS current or power request despite the frequency decline. Its PCC median was 133.076 kW, confirming that the charging-only rule left the 150 kW injection request unmet.

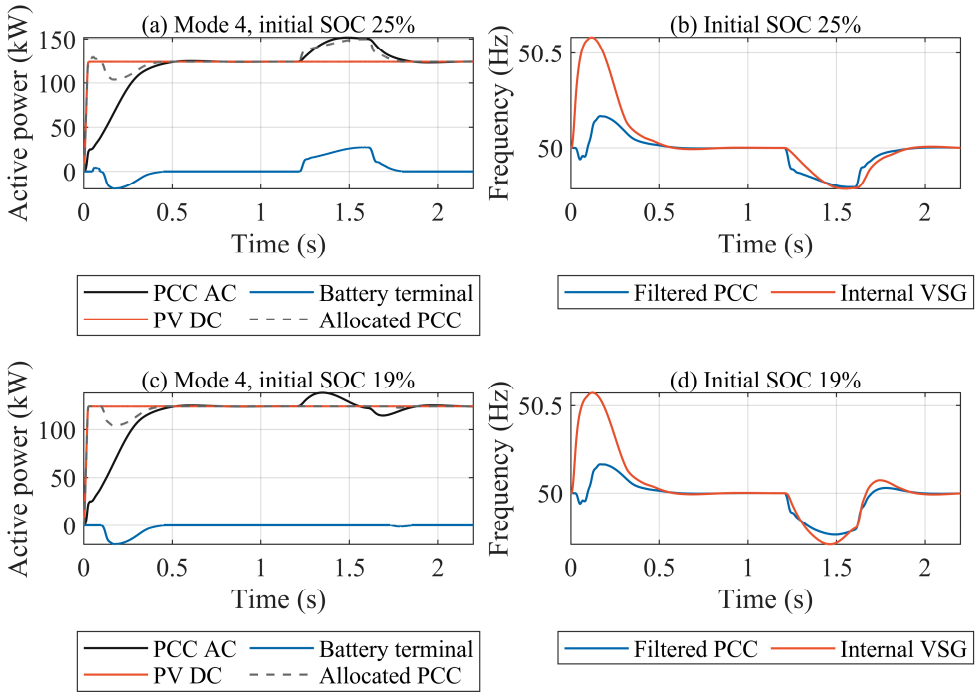



**Figure 14.** Uniform Mode 4 at 600 W/m$^2$: power and frequency for initial SOC of 25% (**a**,**b**) and 19% (**c**,**d**). The latter prohibits commanded discharge throughout. Small native passive terminal power is distinguished from the command.

#### 5.1.5. Mode 5

Figure 15 shows the Mode 5 response. At an initial SOC of 50% and irradiance of 600 W/m$^2$, the recorded mode remained Mode 5. The PCC-power medians in A, B and C were 150.075, 175.843 and 149.859 kW, respectively. The PV remained in MPPT. The battery terminal medians in A and B were 27.248 and 41.994 kW, respectively. In B, the unconstrained frequency request was 26.250 kW, while the additional allocated power was 12.905 kW under the ESS envelope. The simultaneous median PCC-minus-allocated error was 12.937 kW, indicating a transient tracking mismatch.

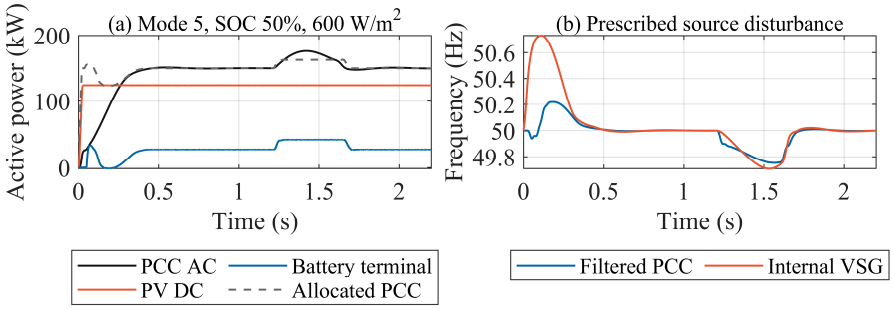



**Figure 15.** Uniform Mode 5 response: (**a**) active power and the allocated PCC target and (**b**) filtered measured PCC and internal VSG frequency. ESS limits constrained the allocated upward reserve.

#### 5.1.6. Quantitative Mode Summary and Inertia Comparison

Table 3 summarizes the uniform mode cases. Every recorded sample satisfied the specified PWM interlock, SOC gates, measured ESS current and 50 kW battery terminal bounds, provisional inverter current bound and applied inertia amplitude and increment bounds. These are checks at the recorded samples; tracking errors were evaluated separately. Seconds-long tests yielded extremely small SOC changes with the specified 5000 Ah storage.

**Table 3.** Uniform-mode window medians. A and B are defined above; tracking error is the median of $P_e$ minus the simultaneous allocated PCC target.

| Mode/Case | $SOC_0$ (%) | Irradiance ($W/m^2$) | $P_e$ A (kW) | $P_e$ B (kW) | $P_{ESS}$ B (kW) | Error B (kW) |
|---|---|---|---|---|---|---|
| 1 | 50 | 800 | 150.079 | 178.769 | 9.596 | 5.145 |
| 2 | 50 | 1000 | 150.081 | 178.770 | −29.319 | 5.155 |
| 3 | 85 | 1000 | 150.078 | 178.766 | 0.014 | 5.144 |
| 4/25% | 25 | 600 | 124.072 | 151.408 | 23.965 | 4.288 |
| 4/19% | 19 | 600 | 124.108 | 133.074 | 0.013 | 9.008 |
| 5 | 50 | 600 | 150.075 | 175.843 | 41.994 | 12.937 |

Table 4 evaluates the 150–120 kW reference step in Figure 10. Bounded adaptive inertia reduced the maximum internal VSG frequency deviation by 5.16% relative to fixed inertia, while power settling took 0.396 s compared with 0.333 s for fixed inertia. The error integral, directional undershoot, 100 ms internal frequency rate and DC-link deviation quantified the associated trade-offs. Applied adaptive inertia ranged from 0.5 to 4.0 kg·m$^2$ and satisfied the 1 ms increment bound. These frequencies describe the internal VSG response to a fixed-frequency source.

**Table 4.** Matched inertia component transient metrics; definitions and evaluation window are given below.

| Metric (1.2–2.2 s) | Fixed $J$ | Bounded Adaptive $J$ |
|---|---|---|
| Maximum internal frequency deviation (Hz) | 0.1807 | 0.1713 |
| Minimum internal VSG frequency (Hz) | 49.8193 | 49.8287 |
| Maximum internal frequency rate, 100 ms (Hz/s) | 1.6124 | 1.6425 |

**Table 4.** *Cont.*

| Metric (1.2–2.2 s) | Fixed $J$ | Bounded Adaptive $J$ |
|---|---|---|
| Power settling time (s) | 0.333 | 0.396 |
| Directional power undershoot (%) | 0.054 | 0.010 |
| Power absolute-error integral (kW·s) | 4.068 | 4.258 |
| Maximum DC-link deviation from 1500 V (V) | 0.295 | 0.281 |

The settling band is the final 120 kW reference ± 0.6 kW (2% of the 30 kW step), and the settling time was measured from 1.2 s to the first sample after the last out-of-band sample. The directional undershoot is (120 kW − minimum PCC power)/30 kW. The power error integral used the absolute error from 120 kW over 1.2–2.2 s. The internal frequency rate used a 100 ms endpoint difference. The DC link values refer to the same post-step window. The initial SOC was 50% in both runs; the final SOC values were 50.000286% and 50.000288%.

#### 5.1.7. Matched Scheduling and DC Link Comparisons

The fixed-MPPT rule baseline changed only the allocation chart from the uniform Mode 2 case. Both shared the physical circuit, initial SOC of 50%, irradiance of 1000 W/m$^2$, adaptive inertia law, deadband, ESS envelope and prescribed source trajectory. The baseline kept the PV in MPPT without deliberate curtailment. Its normal-frequency PCC median was 157.386 kW, compared with 150.081 kW in Mode 2; the low-frequency increases were 28.689 and 29.159 kW, respectively. Table 5 reports the scheduling and transient trade-offs. This matched allocation rule benchmark did not reproduce the complete methods in [3] or [7]. The positive PV power deficit integral integrated the positive difference between the modeled available PV power and measured terminal power over 1.2–2.2 s, combining deliberate curtailment and tracking mismatches.

**Table 5.** Matched uniform Mode 2 versus fixed-MPPT rule. Integrated metrics use 1.2–2.2 s.

| Metric | Mode 2 | Fixed MPPT |
|---|---|---|
| Normal-frequency PCC median (kW) | 150.081 | 157.386 |
| Low-frequency PCC increase (kW) | 28.689 | 29.159 |
| Maximum DC-link deviation (V) | 0.572 | 0.561 |
| Allocated-target error integral (kW·s) | 2.024 | 1.971 |
| Positive PV power deficit integral (kJ) | 5.588 | 1.834 |

The matched Mode 1 pair removed the supercapacitor, its half bridge and the RL branch from the second model, retaining the common DC-link capacitors and other parameters. Figure 11c,d and Table 6 quantify regulation over 1.2–2.2 s. The maximum deviations from 1500 V were 0.479 and 20.715 V for the retained and removed cases, respectively. A settling time of zero means the voltage was already within 1500 ± 1 V throughout the interval, and NR means not reached by 2.2 s. The SC voltage–current integral gave 12.317 kJ of terminal energy exchange. Removing the branch also removed its DC-link regulator, and thus the comparison isolated the contribution of the complete branch.

**Table 6.** Matched supercapacitor branch removal metrics over 1.2–2.2 s. RMS was measured about each window mean; NR means not reached by record end.

| Metric | SC Present | SC Removed |
|---|---|---|
| Maximum deviation from 1500 V (V) | 0.479 | 20.715 |
| Peak-to-peak DC-link voltage (V) | 0.862 | 36.329 |
| DC-link RMS about mean (V) | 0.143 | 10.270 |
| Settling in 1500 ± 1 V (s) | 0 (already in band) | NR |
| SC terminal energy exchange (kJ) | 12.317 | 0.000 |

### *5.2. Recorded Mode Transitions*

Figure 16 uses two separately initialized physical SOC cases. At an SOC of 50%, the prescribed irradiance was 1000, 800 and 600 W/m$^2$ at 0, 1.2 and 2.2 s, respectively; the scheduling category changed from peak to shoulder at 3.2 s. At an SOC of 85%, the irradiance changed from 1000 to 600 W/m$^2$ at 1.2 s, followed by shoulder and off-peak categories at 2.2 and 3.2 s, respectively. The source remained at 50 Hz, and the SOC evolved continuously within each run. The mode entry times were obtained from the recorded mode channel. In the shoulder-period PV deficit, the ESS remained in standby without discharge, and the 150 kW PCC request remained unmet.

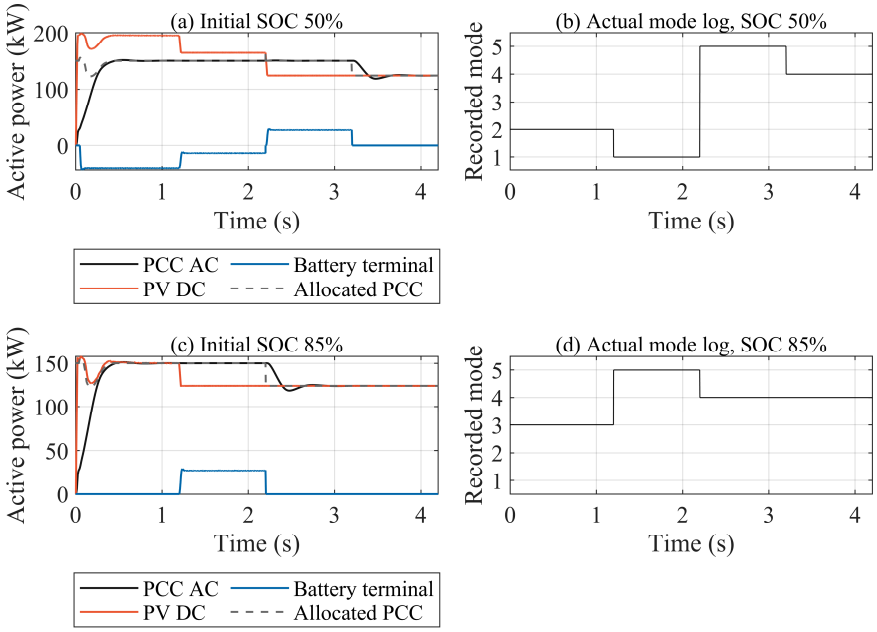



**Figure 16.** Uniform mode transition tests with initial SOC of 50% (**a**,**b**) and 85% (**c**,**d**): active power and actual recorded mode state. Irradiance and scheduling inputs were prescribed; physical SOC evolved continuously within each run. The source remained at 50 Hz.

Table 7 reports settling to the instantaneous allocated PCC target ±0.6 kW until the next recorded mode change or record end. Zero indicates already being in the band at entry. Positive and negative excursions are unnormalized PCC-minus-target errors over the same interval, avoiding undefined percentage overshoot when the base request was unchanged. NR means the error remained outside the band at the last available sample.

**Table 7.** Actual transition times and tracking excursions. Intervals and NR are defined above.

| $SOC_0$ (%) | Mode Change | Entry (s) | Settling (s) | Positive Error (kW) | Negative Error (kW) |
|---|---|---|---|---|---|
| 50 | 2 → 1 | 1.200 | 0.000 | 0.024 | −0.049 |
| 50 | 1 → 5 | 2.200 | 0.007 | 0.484 | −14.120 |
| 50 | 5 → 4 | 3.200 | 0.631 | 25.969 | −5.465 |
| 85 | 3 → 5 | 1.200 | 0.000 | 0.025 | −0.043 |
| 85 | 5 → 4 | 2.200 | 0.627 | 25.940 | −5.498 |

### *5.3. Sensitivity Analysis and Discussion*

The uniform cases spanned initial SOCs of 19%, 25%, 50% and 85% and irradiance values of 600, 800 and 1000 W/m$^2$. Transition tests used changing irradiance values and scheduling categories. A one-factor sweep varied the PCC request to 135 and 165 kW and torque damping to 56 and 84 N·m·s/rad from Mode 1. For damping changes, the allocator slope and compensation used the same varied damping; other settings were retained. Table 8 reports the resulting low-frequency behavior. This sweep evaluated the specified perturbations around the benchmark operating conditions.

**Table 8.** Limited uniform-model sensitivity. Safety refers only to the registered sampled checks; tracking error is reported independently.

| Varied Input | Mode | $P_e$ B (kW) | Error B (kW) | Peak Grid Current (A) | Sampled Safety |
|---|---|---|---|---|---|
| $P_g = 135$ kW | 1 | 163.083 | 4.739 | 350.428 | Pass |
| $P_g = 165$ kW | 5 | 194.291 | 5.322 | 418.527 | Pass |
| $D = 56$ | 1 | 176.455 | 6.461 | 379.482 | Pass |
| $D = 84$ | 1 | 180.760 | 3.588 | 389.824 | Pass |

The numerical checks used pre-specified tolerances of 1% of 150 kW for the PCC-window median differences, 0.01 Hz for the PCC control frequency medians and a 5% relative difference for the current and DC-link deviation peaks. Sampled protection was assessed separately. Figures 11–16 and Tables 3 and 5–8 consistently use the designated 10 µs Tustin switching-interpolation records.

Of the 16 cases compared at 20 and 10 µs, 6 met every numerical and sampled-protection criterion; the remaining 10 retained peak discrepancies above the registered tolerance. All pairs satisfied their recorded-sample protection checks. Additional 5 µs refinements improved some peak estimates but did not establish transient peak convergence: the Mode 3 DC-link deviation peak changed from 0.373 to 0.349 V, a 6.47% difference against the 5% criterion. Numerical peak estimates therefore require caution even where window statistics agree. Supplementary Section S1 gives all retained failures, refinement values and solver warnings.

The independent 500-to-300 A envelope test reached measured peaks of 320.512 and 320.824 A at 20 and 10 µs with a 291 A limited reference, respectively, exceeding the tightened envelope at both periods. The 10 µs record had 13 samples above 300 A. The power recovered to 150 kW ± 0.6 kW 0.278 s after release. Thus, reference limiting did not ensure instantaneous measured-current compliance; this test is distinct from the constant 500 A uniform cases. Supplementary Section S2 reports the full check. Controller-

only input tests verified the applied inertia bounds for the recorded cases, with details in Supplementary Section S3.

The recorded power responses characterize the converter-level allocation under a prescribed source frequency. Network-level disturbance assessment, such as that of Maulà et al. [16], additionally requires a dynamic network and suitable exchanged-power indicators. Likewise, voltage control dynamics and current limiting govern the voltage sag responses examined by Lin et al. [17]. The present frequency-input and envelope tests do not establish network nadir improvement or fault ride-through.

Recent PV–storage VSG work by Zheng et al. combined adaptive inertia with active-loop transient damping compensation [18]. Here, the established inertia component was evaluated within an explicitly constrained PV and ESS allocator. The analysis and simulations address the stated reduced dynamics and short-duration operating cases. TOU categories specify the scheduling contexts; full-day economic savings, battery life benefits and hardware performance remain outside the present validation scope.

## 6. Conclusions

This paper focused on the frequency active response characteristics of PV–storage grid-connected systems and their multi-mode coordinated control strategies. The main research findings are summarized as follows:

- Proposed control architecture: A DC-coupled PV–storage architecture coordinates PV-side MPPT or VCM control, ESS scheduling, DC-link regulation and VSG-based grid-side inverter control. The contribution is the coordination of these functions within a common system-level framework.
- Multi-mode coordinated operation: Five modes coordinate PV control selection with ESS charging, discharging and standby under SOC limits, power constraints and TOU scheduling categories. The scheduling and frequency response requests are combined, subject to direction-specific storage availability.
- Simulation verification: The records quantify PV and ESS allocation in all five modes, SOC-dependent discharge inhibition and actual mode transitions. The matched fixed-MPPT rule identifies scheduling trade-offs, and supercapacitor branch removal quantifies DC link regulation in the specified circuit. Inertia-component comparisons and sensitivity tests characterize the response around the benchmark conditions. The numerical and limiter checks identify the transient peak and measured-current limitations summarized in Section 5.3.

**Supplementary Materials:** The following supporting information can be downloaded at https://www.mdpi.com/article/10.3390/en19215281/s1: Supplementary validation details: Section S1, Numerical verification; Section S2, Inverter current-envelope test; Section S3, Reduced frequency and inertia-controller checks.

**Author Contributions:** Conceptualization, W.X. and Y.Z.; methodology, Y.Z. and W.X.; software, Y.Z.; validation, B.W. and Y.D.; formal analysis, Y.Z.; investigation, B.W. and Y.D.; resources, W.X. and B.W.; data curation, Y.Z.; writing—original draft preparation, Y.Z.; writing—review and editing, W.X. and P.Y.; visualization, Y.Z.; supervision, P.Y.; project administration, W.X.; funding acquisition, W.X. All authors have read and agreed to the published version of the manuscript.

**Funding:** This work was supported by the State Grid Zhejiang Electric Power Co., Ltd. Technology Project under Grant [B311DS240014].

**Institutional Review Board Statement:** Not applicable.

**Informed Consent Statement:** Not applicable.

**Data Availability Statement:** The data presented in this study are available from the corresponding author upon reasonable request.

**Acknowledgments:** During manuscript revision, OpenAI Codex (GPT-6, October 2026) assisted in text revision, simulation and analysis scripts and validation organization. Numerical waveform data were obtained via MATLAB/Simulink execution. The authors retain responsibility for reviewing the models, code, results and manuscript before submission.

**Conflicts of Interest:** Weiwei Xu is affiliated with the Electric Power Research Institute of State Grid Zhejiang Electric Power Co., Ltd., whereas Bingyu Weng and Yongkai Diao are affiliated with the State Grid Ningbo Power Supply Company. The remaining authors declare that the research was conducted in the absence of any commercial or financial relationships that could be construed as a potential conflict of interest.

## References

1. Blaabjerg, F.; Yang, Y.; Kim, K.A.; Rodriguez, J. Power electronics technology for large-scale renewable energy generation. *Proc. IEEE* **2023**, *111*, 335–355. [CrossRef]
2. Zheng, Y.; Luo, Z.; Hua, L.; Li, C. Photovoltaic VSG Coordinated Control System of Source-storage Integration. In *Proceedings of the 2024 4th International Conference on Electrical Engineering and Mechatronics Technology (ICEEMT)*; IEEE: New York, NY, USA, 2024; pp. 185–189.
3. Tran, V.T.; Muttaqi, K.M.; Sutanto, D. A robust power management strategy with multi-mode control features for an integrated PV and energy storage system to take the advantage of ToU electricity pricing. *IEEE Trans. Ind. Appl.* **2019**, *55*, 2110–2120. [CrossRef]
4. Zhang, J.; Qu, L.; Pestana, R.; Luan, F.; Yang, L. Dynamic frequency support by photovoltaic generation with "synthetic" inertia and frequency droop control. In *Proceedings of the 2017 IEEE Conference on Energy Internet and Energy System Integration (EI2)*; IEEE: New York, NY, USA, 2017; pp. 1–6.
5. Wang, L.; Wang, H.; Fu, M.; Liang, J.; Liu, Y. A three-port energy router for grid-tied PV generation systems with optimized control methods. *IEEE Trans. Power Electron.* **2023**, *38*, 1218–1231. [CrossRef]
6. Aghamohamadi, M.; Mahmoudi, A.; Haque, M.H. Two-stage robust sizing and operation co-optimization for residential PV–battery systems considering the uncertainty of PV generation and load. *IEEE Trans. Ind. Inform.* **2021**, *17*, 1005–1017. [CrossRef]
7. Shao, Z.; Bi, Y.; Liang, B.; Li, H.; Wang, Y. Multi-mode energy management method of integrated photovoltaic energy storage system. In *Proceedings of the 2023 11th International Conference on Power Electronics and ECCE Asia (ICPE 2023-ECCE Asia)*; IEEE: New York, NY, USA, 2023; pp. 2706–2712.
8. Thang, T.; Ahmed, A.; Kim, C.-I.; Park, J.-H. Flexible system architecture of stand-alone PV power generation with energy storage device. *IEEE Trans. Energy Convers.* **2015**, *30*, 1386–1396. [CrossRef]
9. Augustine, S.; Ranade, S.J.; Lavrova, O.; De Angelis, V.; Cowles, G.; Huang, J.; Wittman, R.; Atcitty, S.; Pragallapati, N. Inverter-Agnostic DC-Coupled Solar+ Storage System. *IEEE Access* **2025**, *13*, 207033–207046. [CrossRef]
10. Dong, W.; Diao, H.; Xu, J.; Kang, J.; Lv, Z. Analysis and parameters design of grid-forming converter for enhancing the stability of photovoltaic storage system under weak grid. *IEEE Access* **2024**, *12*, 134273–134284. [CrossRef]
11. Huang, Y.; Fang, Z.; He, Z.; Wang, D.; Tang, J.; Xie, C.; Zhou, K. Impacts of interactions between grid-forming and grid-following converters on stability of hybrid system connected to weak grid. In *Proceedings of the 2024 IEEE 7th International Electrical and Energy Conference (CIEEC)*; IEEE: New York, NY, USA, 2024; pp. 2183–2188.
12. Baškarad, T.; Holjevac, N.; Kuzle, I. Photovoltaic system control for power system frequency support in case of cascading events. *IEEE Trans. Sustain. Energy* **2023**, *14*, 1324–1334. [CrossRef]
13. Li, X.; Hui, D.; Lai, X. Battery energy storage station (BESS)-based smoothing control of photovoltaic (PV) and wind power generation fluctuations. *IEEE Trans. Sustain. Energy* **2013**, *4*, 464–473. [CrossRef]
14. Chen, Y.; Xia, Y.; Li, H.; Yang, K.; Li, D.; Fan, Y. Adaptive VSG grid-connected control strategy based on moment of inertia and damping coefficient. In *Proceedings of the 2024 IEEE 7th International Electrical and Energy Conference (CIEEC)*; IEEE: New York, NY, USA, 2024; pp. 4583–4588.
15. Shen, H.; Chen, Z.; Ren, B.; Chen, A.; Shi, M.; Huang, Z. Modeling and Parameter Identification of the Photovoltaic Inverter based on VSG. In *Proceedings of the 2022 7th Asia Conference on Power and Electrical Engineering (ACPEE)*; IEEE: New York, NY, USA, 2022; pp. 717–722.
16. Maulà, G.; Savastio, L.P.; Amato, G.; Abdollahi, A.; De Tuglie, E.E. Characterization of disturbances induced by a microgrid on the distribution network. *Sustain. Energy Grids Netw.* **2025**, *43*, 101843. [CrossRef]

17. Lin, M.; Zhang, L.; Yang, Q.; Mansour, D.-E.A.; Zobaa, A.F. Analytical characterization of grid-forming converter response time under voltage sags. *IEEE Trans. Power Electron.* **2026**, *41*, 12615–12621. [CrossRef]
18. Zheng, Y.; Xu, Y.; Yang, Y.; Hua, L.; Yang, Y. Application of adaptive virtual synchronous generator based on improved active power loop in photovoltaic storage systems. *Front. Energy Res.* **2025**, *12*, 1468629. [CrossRef]

**Disclaimer/Publisher's Note:** The statements, opinions and data contained in all publications are solely those of the individual author(s) and contributor(s) and not of MDPI and/or the editor(s). MDPI and/or the editor(s) disclaim responsibility for any injury to people or property resulting from any ideas, methods, instructions or products referred to in the content.